Journal of Petroleum Exploration and Production Technology (2020) 10:3827–3848
https://doi.org/10.1007/s13202-020-00904-6

ORIGINAL PAPER - PRODUCTION ENGINEERING

Investigating the effects of fault reactivation and CO_2 migration during combined CO_2-EOR and sequestration within a mature oil reservoir

Shawn Pulchan[1] · David Alexander[1] · Donnie Boodlal[1]

Received: 13 December 2019 / Accepted: 5 May 2020 / Published online: 23 May 2020

Abstract

The investigation into the combined processes of CO_2-EOR and geologic carbon sequestration was seen to be a viable solution to reducing CO_2 emissions from the atmosphere, while boosting production from mature oil fields. However, the practicality of the combined process hinges on the determination of an optimum injection pressure to maximize the application of both methods. In addition, the success of these two operations is also contingent upon the dynamic sealing capacity of bounding faults, to allow hydrocarbon accumulation and trapping of injected CO_2. Consequentially, the goal of this research is to optimize the implementation of combined CO_2-EOR with simultaneous CO_2 sequestration and investigate the enhancing/diminishing aspects of fault reactivation and CO_2 migration. The study was approached from two scenarios; the first was the determination of an optimum injection pressure for the combined process, with the main focus on maximizing recovery from a mature oil field. The results saw a maximum cumulative recovery of 73.7090 Mbbls being facilitated at an optimal injection rate of 722 Scf/day. The second scenario entailed the investigation of the occurrence or lack thereof, of injection-induced fault reactivation at this predetermined injection rate of 722 Scf/day. Simulations reflecting the characteristics of fault reactivation were conducted, and are indicative of relations between fault opening stress, reactivation time, hydraulic fracture permeability, fracture propagation length, and leakage. Conclusively, the viability of the combination of CO_2-EOR and sequestration were seen to depend on the technicalities of fault reactivation. In some cases, reactivation resulted in increases of accessible storage capacity, whereas, in other instances, it led to the leakage of the injected CO_2.

Keywords Fault reactivation · CO_2 sequestration · Enhanced oil recovery · CO_2 migration · Mature oil reservoir · Barton–Bandis fracture permeability theory

List of symbols

khf	Hydraulic fracture permeability (md)
kccf	Fracture closure permeability (md)
krcf	Residual fracture permeability (md)
frs	Fracture opening stress (psi)
kf	Fracture permeability (md)
σ'_n	Effective normal stress (psi)
σ	Stress (psi)
P_p	Pore pressure (psi)
MM	10^6 (–)
Scf	Standard cubic feet (–)
PV	Pore volume (Scf)
S_{grm}	Maximum residual gas saturation (fraction)
$\varnothing$	Porosity (fraction)
lb	Pound (–)
ft	Feet (–)
k	Permeability (md)

Introduction

In the recent past, Trinidad and Tobago has ranked as one of the world's leaders for carbon dioxide emissions per capita. In 2016, the country was among the top 10 emitters per capita globally, competing with energy gluttons such as Kuwait, Qatar, and the UAE (The National Gas Company of Trinidad and Tobago 2019). In 2018, according to The Global Carbon Atlas (2018), the country's total territorial carbon dioxide emissions amounted to 44 million tonnes, a staggering valuation in relation to the diminutive size of the

✉ Shawn Pulchan
shawn.pulchan@hotmail.com

[1] University of Trinidad and Tobago, Point Lisas, Trinidad and Tobago

country (population = 1,389,843). However, the country is showing intentions of transitioning to a more environmentally conscious society. In keeping with this outlook, the country deposited its instrument of ratification to the Paris Agreement on climate change on February 22, 2018, which detailed the country's commitment to reducing cumulative greenhouse gas emissions by 15%, by the year 2030. Notwithstanding this intended commitment, if the need arises for safer, more efficient methods of carbon dioxide removal in the future, preferences should be readily available. In such an instance, there exists a multitude of diverse solutions to address this growing concern. However, the injection of carbon dioxide into subsurface depleted hydrocarbon reservoirs is considered one of the more plausible solutions to address the increasing concentration of greenhouse gases within the atmosphere, all while enhancing oil production. In light of such, a simple source/sink analysis helps to contextualize Trinidad and Tobago's prospects of possible geologic carbon sequestration. The country's total proved natural gas reserves as of 2018 amount to 11.24 TCF (Knoema 2019). This conveys that a possible several hundred million tonnes of carbon dioxide, equivalent to a few decades of domestic emissions, can be sequestered within depleted natural gas reservoirs. Such a revelation, therefore, emphasizes the applicability of geologic carbon sequestration as a substantive emission mitigation approach for the country and hence forms part of the motivation behind this study.

Four potential carbon dioxide storage systems can be associated with mature oil reservoirs, which include structural, residual, solubility and mineral trapping. Of those previously mentioned, structural trapping is seen to have the most significant effect on storage volumes as it entails the trapping of free gas when it encounters impermeable layers of cap or faulted rock, which acts as a seal. Consequently, the long-standing integrity and practical storage capacity of these reservoirs are therefore contingent upon the sealing rock's durability and geomechanical integrity of adjoining faults. However, on account of a fault often having a sealing capacity in an order of magnitude lower than the top seal within a particular storage site, the emphasis was placed on investigating fault sealing capacity and forms an integral part of this research. Fault sealing degradation may arise as a result of increased pressure due to prolonged carbon dioxide injection into a storage site, which may alter the pre-existing stress field around injection wells and prompt fault reactivation. Therefore, for any carbon dioxide sequestration project, it is necessary to appraise and interpret the possible implications of carbon dioxide injection on the dynamic sealing and yielding capacity of neighboring faults, and thus indirectly on storage. For a sequestration process, maximizing the quantity of permanently stored carbon dioxide is the primary focus. In essence, this storage quantity is solely based on the capacity available for storage, which can either be enhanced or diminished by fault reactivation via migration.

Furthermore, this process of carbon dioxide sequestration prompted by the necessity of avoiding carbon dioxide emissions can also be combined with the possibility of simultaneously increasing oil production from a mature field. This process is regarded as carbon dioxide enhanced oil recovery and in essence, primarily focuses on maximizing the volume of oil recovered through additional pressure maintenance. For operation within mature reservoirs which are typically severely depleted, this pressure maintenance is facilitated at high injection rates. However, for the combined approach with carbon dioxide sequestration, it is necessary to obtain an optimal injection pressure at which recovery will be optimized while either forestalling or cultivating fault reactivation and leakage to maximize storage. This pinpoints the merit upon which the research was conducted, and the above underlying statement was investigated within the Point Fortin/Cruse area (southwestern Trinidad) via the use of fluid flow and geomechanics coupled reservoir simulation.

The goal of this research is to (1) determine the optimum injection pressure for the combined process of CO_2-EOR and geologic carbon sequestration within a mature oil reservoir, (2) quantify the leakage of CO_2, and/or, the constituent volumes of CO_2 associated with each type of trapping within the injected formation, (3) capture the characteristics of fault reactivation and yield using simulation models constructed in the GEM suite of the commercial reservoir simulator CMG, (4) compare these various faulted reservoir models to observe the effects of fault reactivation and CO_2 migration on storage capacity, (5) simulate variations in fracture permeability of the fault to characterize the effects on reactivation time and leakage.

Geologic setting

The prospective field is located in the Cruse area, locally centered around the borough of Point Fortin and spans the combined acreage of three fields—Point Fortin Central, Point Fortin East, and the Cruse Fields (Fig. 1). The area consists of internal major and minor fault complexes, roughly circumscribed by two north-west/south-east trending faults, disciplined by seismic activity which is seen to be associated with the major Los Bajos Fault system. More specifically so, it is situated just north of the Los Bajos fault system and runs along the northern flank of the east–west trending Point Fortin anticlinal feature. The affiliated structure is that of north–north-east, gradual non-uniform dipping anticline limits, ranging from 45° in the south, to 4° north–north-east in the down dips locations to the north and east. Water levels in this down-dip position in conjunction with shale outs, limits the reservoir

Fig. 1 Petrotrin thermal map depicting the location of the Cruse 'E' field (adapted from Ramlal 2004)

to the east, while shaling outs provide reservoir closure to the north and south. The main focus is the uppermost section, of the Upper Cruse formation which is seen to be Pliocene of age. It is representative of a major regressive deltaic sequence, characteristic of deposition within a high stand system tract. The lower Forest clay forms a thick shale sequence which unconformably overlays the objective sands. These clays are indicative of the upper transgressive system tract and form an effective upper seal for the reservoir. These reservoir objective sands are rendered to comprise of north-east/south-west trending distributary channel/mouth bar complexes, indicative of deposition in a lower deltaic plain environment.

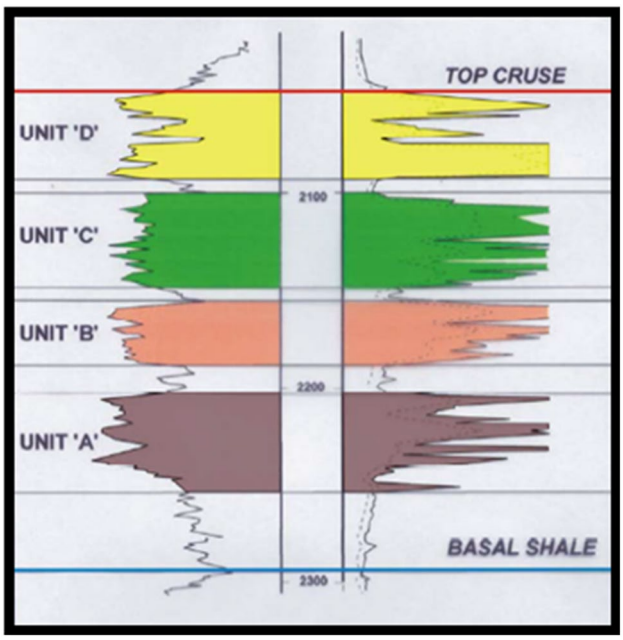

Fig. 2 Cruse 'E' type log - CRUSE 166 (adapted from V. Ramlal 2004)

Lithologically, the Cruse 'E' sands forms part of an alternating sand and shale sequence, located at an average depth of 1800 feet, with average net sand oil thickness of 150 feet. It comprises of a series of several stacked discrete mappable, elongate reservoirs, containing distinct shale out edges. These objective sand intervals are categorized into four distinct mappable units arranged stratigraphically from lowermost unit 'A' to the uppermost unit 'D,' each separated from the overlying and underlying unit by distinct shales. This stratigraphic sequencing can be observed form a type log of Cruse 166 (Fig. 2).

Isopach maps of these Upper Cruse sand units are identified primarily by a particular arenaceous foraminiferal assemblage that occurs below the Top Cruse surface and limited at the base of the first fining upward, retrogradational sand, occurring just below the Lower Forest clay.

Table 1 Cruse 'E' (IADB) expansion steamflood summary of reservoir (adapted from SPE 89411—Ramlal 2004)

Reservoir property	Value
Average sand depth (ft)	1800
Average reservoir temperature at the start of steamflood (°F)	110
Average crude oil viscosity at reservoir conditions (cp)	175
Crude gravity at 60 °F (°API)	16-18
Average permeability (md)	265
Average sand thickness (ft)	75
Average porosity (%)	31
Area (Acres)	270
Initial oil saturation (%)	75
Estimated oil saturation at start of steamflood (%)	68
Formation volume factor (Res bbl/stb)	1.1
Original oil in place at the start of steamflood (MMBBL)	31.1

These four oil-sand isopach maps labelled Unit 'A' through 'D' were adapted from SPE 89411—V. Ramlal, 2004, and depicts best sand development occurring in Unit 'B' and 'C'. Additionally, a summarized reservoir description via petrophysical properties can be observed within Table 1.

Theory

Overview of CO_2-EOR and sequestration

Carbon Capture and Sequestration involves a three-stage process whereby carbon dioxide gas is trapped and otherwise avoided form being emitted into the atmosphere, in order to facilitate its storage in deep geologic formations within the subsurface. These three main stages include capture, transport and utilization/safe storage. The capturing aspects of the process entail the trapping of carbon dioxide and sometimes also include separation from other gases produced at large-scaled industrial process facilities. Once separated, it is compressed and transported via trucks, ships or pipelines to suitable sites for geological storage. At these sites, the carbon dioxide gas is injected into deep subsurface rock formations, usually at depths in excess of one kilometer. These subsurface rock formations then act as repositories for the injected gas. These usually include unminable coal seams, deep saline aquifers and depleted oil/gas reservoirs. On the opposing end of the spectrum, carbon dioxide enhanced oil recovery involves the injection of carbon dioxide gas into an oil reservoir, often with intervening periods of water injection, exclusively for the purpose of improving the flow of oil out of the reservoir (Advanced Resources International and Melzer Consulting 2010), and thus ultimately maximizing recovery. This injected carbon dioxide acts to reduce the viscosity of the oil and improve the recovery efficiency of the remaining unproduced oil, therefore facilitating an increase in produced oil. Some of this injected carbon dioxide is recovered with the produced oil; however, a portion also remains permanently trapped within the reservoir. Once the maximum recoverable oil is produced, injection may be continued to increase the amount of carbon dioxide that can be permanently stored in the depleted reservoir.

This commonality of carbon dioxide storage associated with both processes, therefore, forms the basis upon which both singular methods can be combined into a dual process associated with the operation within a mature/depleted oil reservoir. In light of such, carbon dioxide storage is facilitated via various types of trapping which include structural/stratigraphic, residual-gas, solubility and mineral trapping. Initially, the injected carbon dioxide is primarily trapped by physical mechanisms, that is, either by structural/stratigraphic or by hysteresis (residual-gas). Eventually, over extended periods of time, storage security increases via the action of solubility or mineral trapping.

Operation of the Barton–Bandis fracture permeability model in conjunction with the dual permeability model

The practicality of combined production and sequestration practices rely critically on the fact that the producing formation responds dynamically to changes in applied stresses. Specific to this study, these may include plastic deformation, shear dilatancy, compaction drive and injection-induced fracturing. In such instances, a coupled geomechanical model consisting of submodels can be used for simulating these aforementioned responses. Coupled geomechanics modelling can be utilized for a range of simulative situations. As it relates to this study, these include the geomechanical effects of rock deformation within a geological setting as well as, the determination of leakage through points of weakness in caprock during carbon dioxide sequestration. These geomechanical effects which prompt changes in matrix and fracture permeability can be computed by a number of algorithms such as those proposed by Li and Chalaturnyk: and Barton–Bandis (C.M.G Ltd. 2016). For the purpose of this study, we will utilize the Barton–Bandis fracture permeability submodel in conjunction with the dual permeability submodel to simulate these aforementioned effects, of which, a brief overview of the theory and operation is discussed below.

Generally, for the model construction process, a natural-fracture grid option for fluid flow comprises of the usual grid system for the porous rock matrix, coupled together with a second grid system. This second grid system incorporates fracture blocks that synchronize with the matrix blocks on a one-to-one basis. This dual grid system is implemented

for the construction of two submodels: a dual permeability submodel in conjunction with a geomechanical submodel.

The incorporation of this dual permeability sub modelling approach allows reservoir models to comprise of two permeability systems to constitue a grid block: similarly, a matrix system and a fracture system. This allows grid blocks to comprise of one matrix permeability (carrying a MATRIX qualifier) and one fracture permeability (carrying a FRACTURE qualifier) where the matrix is connected to the fracture in the same grid block. In a similar sense, the dual grid system allows all geomechanics calculations to be coupled solely to the matrix blocks. However, fracture opening and closing associated with the fracture blocks may be dependent upon stresses within the matrix blocks. That is, the use of one type of qualifier over the other in the dual permeability submodel would be influenced by the geomechanical conditions within the specific matrix block. Therefore, under appropriate geomechanical submodel conditions, this dual permeability formulation assumes that matrix blocks are adjacently connected to one another, and thus provides channels for fluid flow, indicative of points of weakness or fractures.

This link between the geomechanical submodel conditions and the dual permeability grid block value is then made via the use of the Barton–Bandis model. This allows for the calculation of the fractured block permeability from the normal fracture effective stress and as such, the fracture permeability is dependent on the value and history of normal fracture effective stress as depicted in Fig. 3.

Moreover, for a sealing fault, initially effective normal stress is higher than fracture opening stress, as depicted by path AB on Fig. 3. On this path, the fracture permeability is minimal as depicted in relation to the y-axis on Fig. 3, and behavior is reversible. As injection commences and prolongs, an increase in pore pressure prompts a decrease in the effective normal stress, in accordance with the following relationship where σ'_n (effective normal stress), σ (normal stress) and P_p (pore pressure):

$$\sigma'_n = \sigma - P_p$$

When the effective normal stress, becomes less than or equal to the fracture opening stress (i.e., moving from point A to point B as depicted on Fig. 3), the fracture opens suddenly, and permeability drastically increases to hydraulic fracture permeability (indicative of fault reactivation) as depicted by path BC on Fig. 3. As long as the effective normal stress is less than zero and the fracture opening stress, the fracture remains open, and permeability stays at hydraulic fracture permeability, that is along path DE as depicted on Fig. 3. When the effective normal stress becomes greater than zero and fracture opening stress, the fracture will close and the fracture permeability will jump from hydraulic fracture permeability to fracture closure permeability, that is along path EF as depicted on Fig. 3. Thereafter, fracture permeability varies reversibly with effective normal stress on path GFED as depicted on Fig. 3.

Methodology

Three-dimensional GEM sector model

The base map file representative of the field model was constructed using the well pattern map (Fig. 4), the structure map of top Cruse (Fig. 5), both presented below. The pattern map was superimposed on the structure map to facilitate the plotting of well locations on the structure map. The base field map was then digitized using the Didger 5 software to

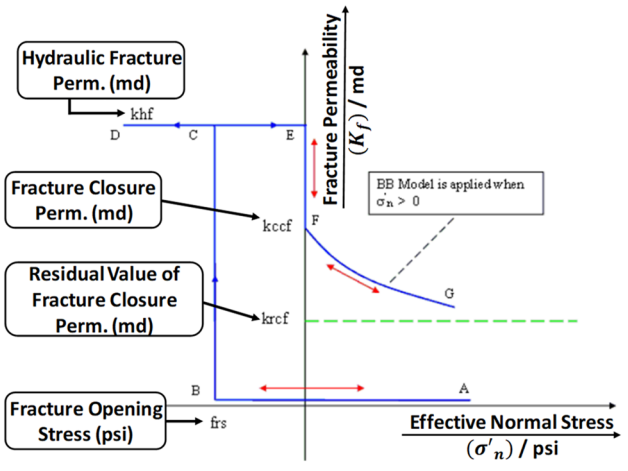

Fig. 3 Automatic alteration of fracture permeability under the operation of the Barton–Bandis theory (adapted from CMG-GEM manual, 2016)

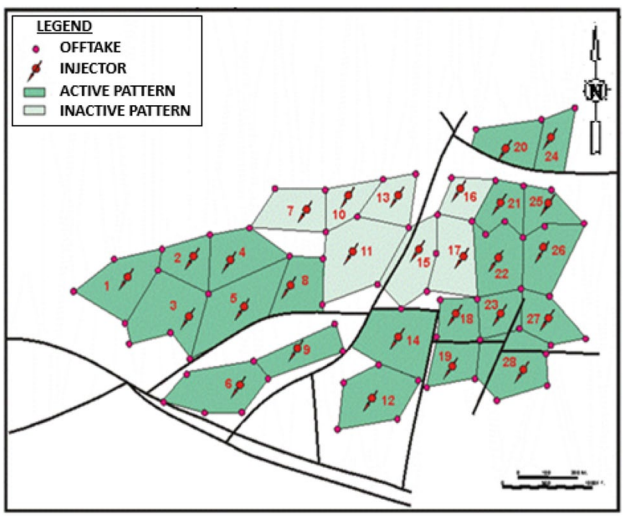

Fig. 4 Well pattern map (adapted from SPE 89411—Ramlal 2004)

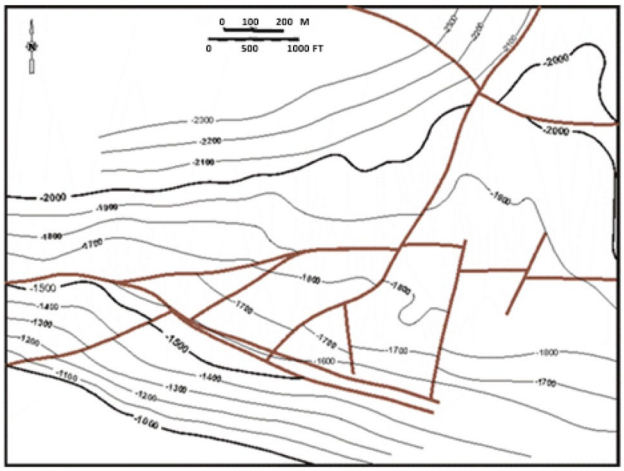

Fig. 5 Structure map of top Cruse (adapted from SPE 89411—Ramlal 2004)

produce an exportable Excel datasheet. This excel data was then used to construct relevant base data files for Contours/Structure, Wells, Faults and a Boundary. These files were then imported into the Petrel software and used to create the initial geo-model of the field. Within the Petrel software, each fault included in the model was defined by tracing the respective shape of each. A grid was then constructed using the 'Pillar Gridding' process to produce a 'skeleton grid' defined by all the faults and pillars. Vertical layering of this three-dimensional faulted grid was then implemented via creating horizons. The end result of these steps saw the creation of a geo-model representation of the field. Petrophysical filed data was then added to this geo-model to produce a resultant petrophysical model. This was implemented via the interpolation of continuous data throughout the previously constructed geo-model grid. Varying distributions for Net-Pay, Porosity, and Oil-Saturation were populated. Each property was distributed against input trend data obtained from four Net-Oil-Sand Isopach maps adapted from SPE 89411—V. Ramlal, 2004, and are indicative of each sand layer within the reservoir.

This fully populated three-dimensional grid was then exported to a joint industry format model referred to as a RESCUE model, which provided a forum for the transfer of data from the three-dimensional petrel reservoir model. This rescue model was then imported into the IMEX suite of the commercial reservoir simulator CMG to reproduce a copy of the three-dimensional grid system inclusive of properties, fault surfaces, and wellbore trajectories. This grid system was then fully populated with the following submodels; a reservoir properties description, filled with data presented within Table 1. A fluid component model created via the quick black oil option of the IMEX suite. A rock fluids model defined by water–oil and liquid–gas relative permeability curves. An initial conditions description of the reservoir using the 'USER INPUT' option, and, a well recurrent section. A conversion from IMEX to a STARS field model was then implemented to allow for the simulation of thermal results—to be used in model validation.

The model was validated via a CMOST history match against field history data, which can be observed in Fig. 6. This validated STARS field model was then converted to a GEM field model to facilitate the substantive investigation of carbon dioxide injection and storage. This conversion then prompted the creation of a WINPORP fluid submodel, which was generated in accordance with compositional data retrieved from Sobers et al. (2011), as presented within Table 2. The inclusion of this WINPROP generated fluid model saw the creation of the three-dimensional GEM field model. From this field model, an arbitrary grouping of grid blocks were chosen to constitute a sector model as depicted in Fig. 7. This three-dimensional GEM sector model was then used to investigate the optimal carbon dioxide injection pressure associated with a carbon dioxide enhanced recovery process within a depleted reservoir. A summary of the methodology workflow for the construction of and the investigation on the three-dimensional sector model can be observed in Fig. 8.

Two-dimensional GEM block model

A simple two-dimensional block model was constructed in the GEM suite of the commercial reservoir simulator—CMG, to represent a thin two-dimensional homogenous segment of the larger GEM field model. As a result, the model follows the same lithological sequencing and was populated using the same submodels as discussed above. The inclusion of a vertical fault which intersects the entire thickness of the reservoir is implemented to investigate fault reactivation. It consists of a single producer located within the fault, which is perforated at the topmost layer in order to quantify any leakage to surface of the injected carbon dioxide as a result of fault reactivation. Also, an injector which implements carbon dioxide injection to stimulate reservoir pressurization is placed at the rightmost grid block, furthest away from the fault. Moreover, the model implements a 'Dual-Permeability' grid system in order to apply the 'Barton–Bandis' Fracture Permeability' option to simulate permeability increase as a representation of fault reactivation. The incorporation of the Barton–Bandis submodel to the two-dimensional reservoir model saw the addition of specific fracture properties as presented within Table 3. A summary of the methodology workflow for the construction of and the investigation on the two-dimensional block model can be observed in Fig. 8.

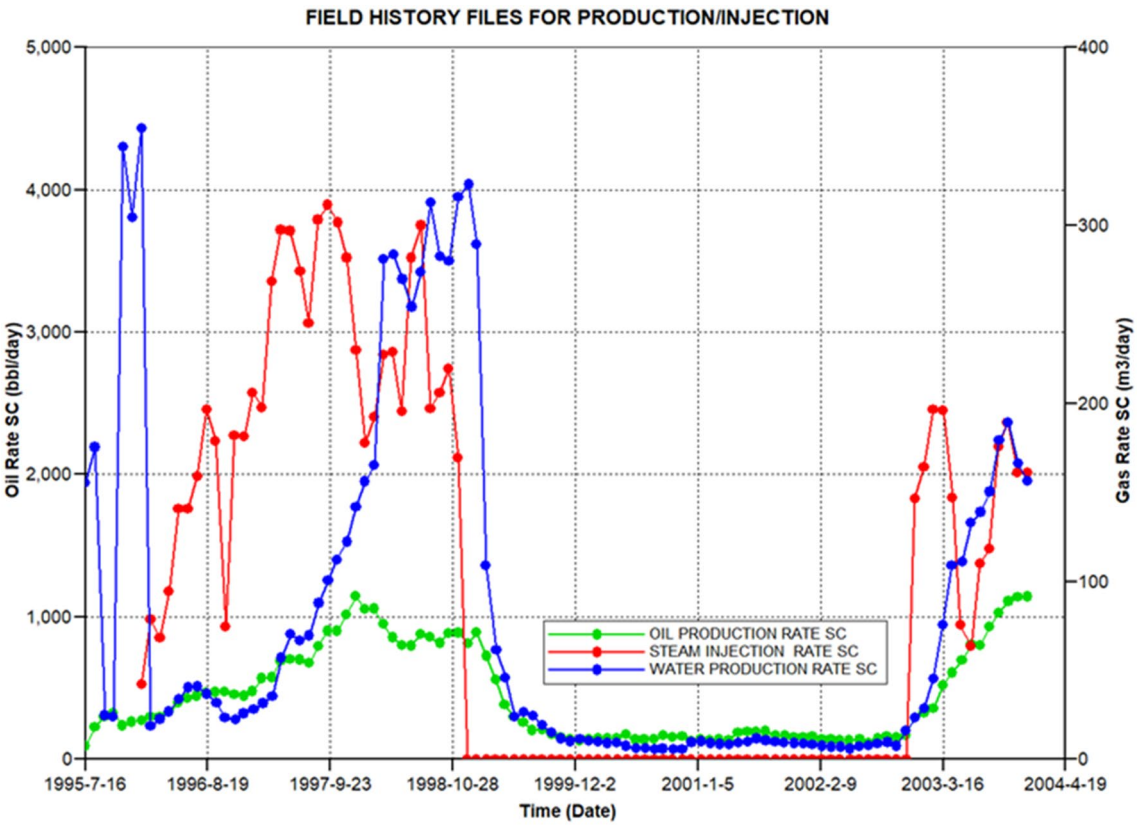

Fig. 6 Filed history data for oil production, water production and steam injection

Table 2 Compositional description of crude oil components used in the generation of the Winprop Black Oil model (adapted from SPE 147141-MS—Sobers et al. 2011)

Crude gravity	Compositional description of crude oil components								
	Component	Mole (%)	Weight (%)	MW (g/mol)	P_{crit} (Atm)	T_{crit} (k)	Omega A	Omega B	Acentric factor
17.6° API	CO_2	0.92	0.23	44	72.904022	304.7	0.45724	0.0777796	0.225
	C_1	42.80	3.90	16	45.437947	190.6	0.42724	0.077796	0.013
	C_1–C_6	14.82	4.47	53	50.658771	495.7	0.52817	0.11669	0.182
	C7+	41.46	91.36	388	14.478164	1196.3	0.39142	0.08391	0.805

Results and discussion

Optimizing CO_2 injection rate for oil recovery and quantifying storage and/or leakage

The three-dimensional sector model used in this aspect of the study incorporated all the previously populated reservoir rock and fluid properties as discussed above. However, a structural alteration was implemented to provide a valid geological approach to investigate the optimum injection pressure of carbon dioxide enhanced oil recovery in conjunction with simultaneous sequestration. This edit consisted of splitting the topmost sand layer, Unit D into two additional layers. The addition of these two layers saw the creation of a ten feet cap rock layer and a one-foot sand layer included as the topmost layer. The sector formation laterally spans 3619 feet in length and 1709 feet in width, with an oil in place of 7.545 MMBbls. Similar to the field model, it has a formation thickness of 299 feet and is penetrated by forty-two wells, fourteen of which are injectors and the remaining twenty-eight are producers. The model sees the effect of two faults, which are inherited from the primary field model, one of which bisects through the entire width of the sector model. An additional producer perforated at this topmost sand layer

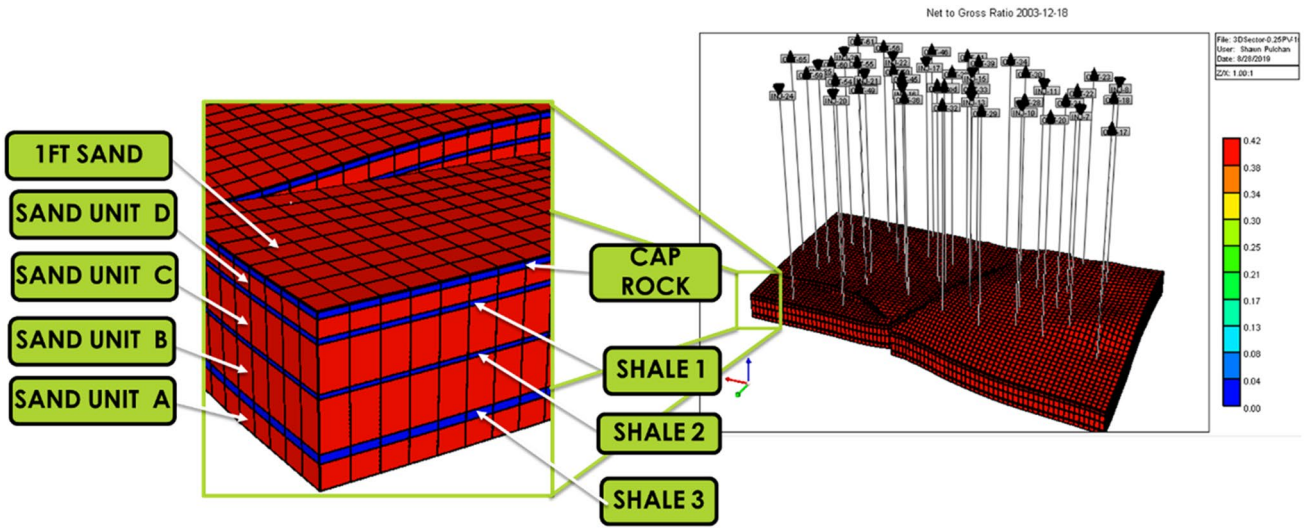

Fig. 7 Final three-dimensional GEM sector model for optimizing oil recovery and evaluating storage/leakage

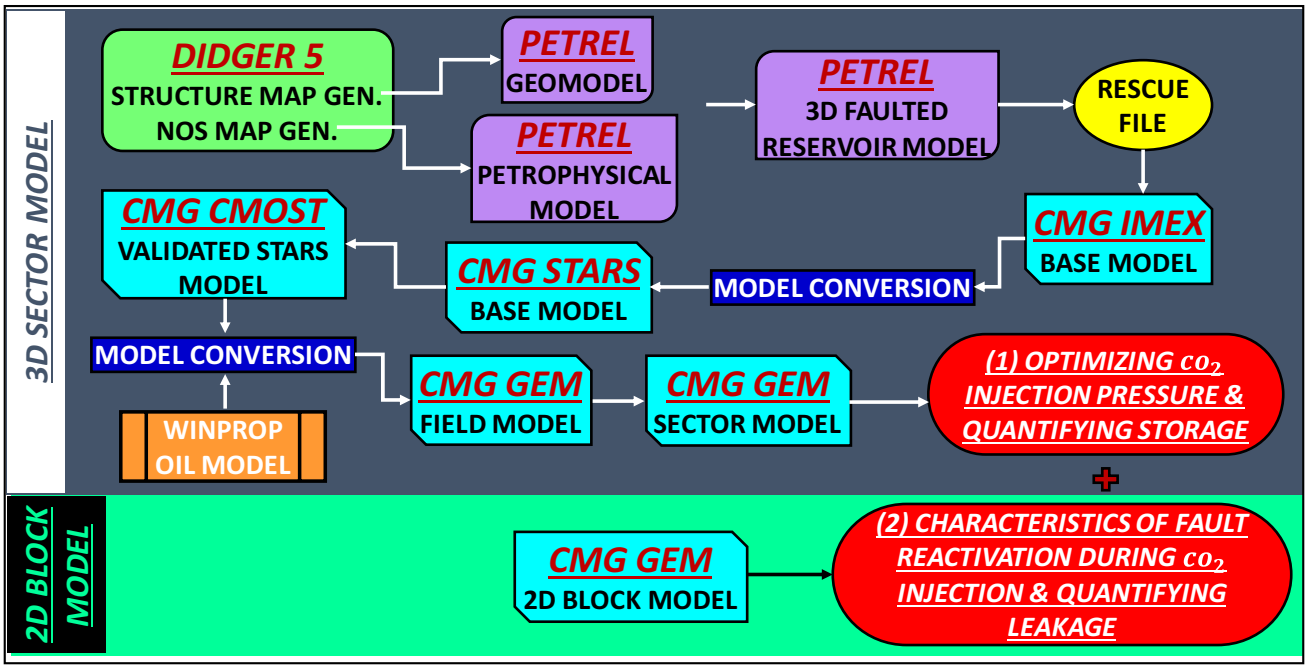

Fig. 8 Methodology workflow implemented within the study

is also included for the purpose of quantifying leakage. The resultant model can be observed in Fig. 7.

Optimum injection rate

The investigation of the optimum carbon dioxide injection rate was conducted exclusively on the basis of maximizing oil recovery from the sector model. As a result, various injection strategies were implemented on a pore volume basis at varying producing drawdowns. The calculation below shows the computation of the injection rate corresponding to one pore volume.

Total HC pore volume of sector model; 73.8105 MMScf
Intended duration; 5 years
Total number of injectors within sector; 14

Table 3 Summary of Barton–Bandis fracture properties implemented on the two-dimensional block model

Fracture properties	Value
Eo—Initial fracture aperture	6.5×10^{-5} ft
Kni—Initial normal fracture stiffness	2.999921×10^{6} psi/ft
FRS—Fracture opening stress	100 psi
Khf—Hydraulic fracture permeability	500 md
Kccf—Fracture closure permeability	500 md
Krcf—Residual value for fracture closure permeability	500 md

Table 4 Various injection strategies implemented to optimize oil production

Injection strategy	Injection rate
0.25 pore volume	722 Scf/day/Inj
0.50 pore volume	1444 Scf/day/Inj

$$\text{Injection rate @ 1 pore volume} = \frac{73.8105 \times 10^{6}\ \text{Scf}}{365\ \text{Days} \times 5\ \text{Years} \times 14\ \text{Inj}} = 2889\ \text{Scf/day/Inj}$$

Table 4 below depicts the resultant injection rates corresponding to each pore volume injection strategy. These injection strategies were implemented at varying producing drawdowns in an attempt to extract the maximum volume of oil out of the reservoir under the given conditions. Carbon dioxide injection was facilitated through 14 active injectors, while the oil recovery was implemented by 28 producers. In addition to this approach, two simulations of water-alternating- gas injection were implemented, the first at a 1:1 ratio and the second at a 2:1 ratio. With respect to the water-alternating-gas strategies, water injection was facilitated initially, followed by carbon dioxide injection. The result of this investigation can be observed in Fig. 9. The actual cumulative productions associated with each injection/production strategy investigated can be observed in Table 5. Based on the values outlined in Table 5, the optimum injection strategy was chosen as an injection at 0.25 pore volume, at a producing drawdown of 15 psi. This selection was made on the basis of maximum oil recovery as well as the economic viability of the procedure. In such a sense, this injection strategy is seen to inject a lower volume of gas, at the same producing drawdown and recovers approximately the same volume of cumulative production. This lower volume of injected gas equates to a reduction in the expenditure associated with obtaining the carbon dioxide and operating the injection. Therefore, conclusively, the three-dimensional sector model is observed to relay a maximum cumulative

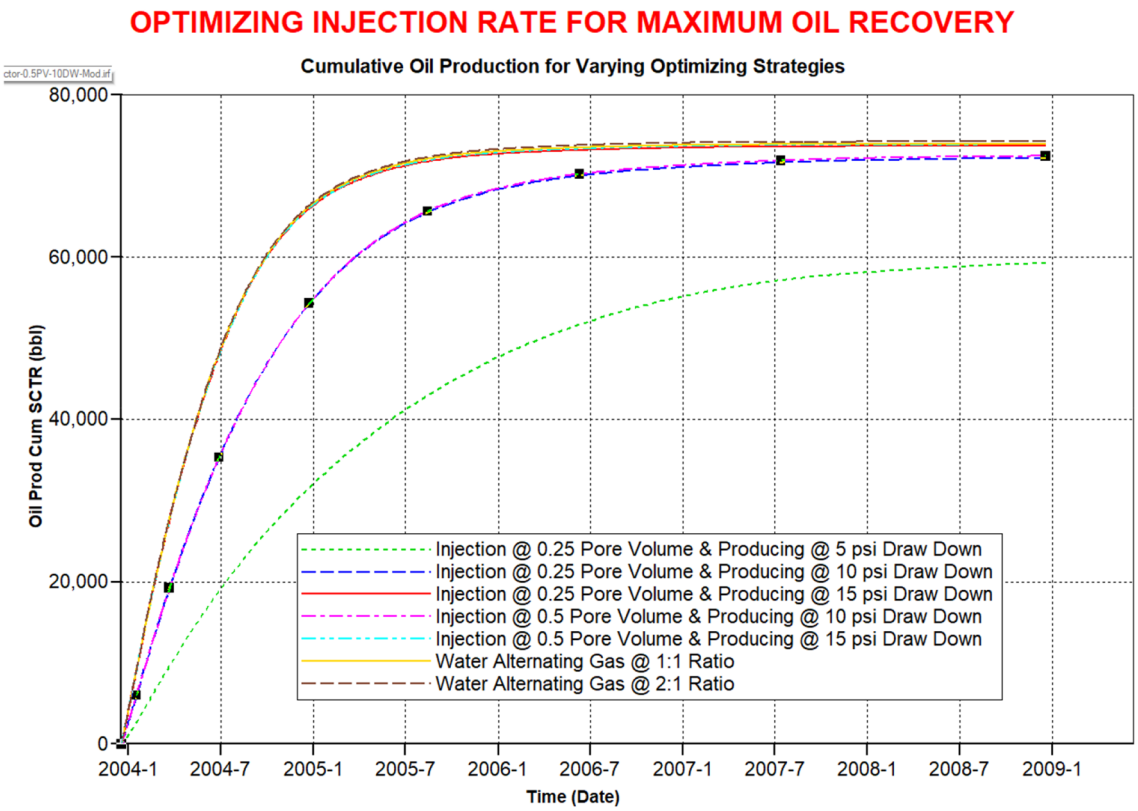

Fig. 9 Cumulative oil production response for varying optimization strategies

Table 5 Actual cumulative volumes in response to varying injection/production strategies for optimizing oil recovery

Injection strategy	Production strategy	Cumulative oil production (Mbbls)
0.25 pore volume = 722 Scf/day	5 psi drawdown	59.2768
0.25 pore volume = 722 Scf/day	10 psi drawdown	72.1729
0.25 pore volume = 722 Scf/day	15 psi drawdown	73.7090
0.50 pore volume = 1444 Scf/day	10 psi drawdown	72.4546
0.50 pore volume = 1444 Scf/day	15 psi drawdown	73.8963
WAG 1:1 (0.25 PV_W × 30 days:0.25 PV_CO_2 × 30 days)	15 psi drawdown	73.9565
WAG 2;1 (0.25 PV_W × 60 days:0.25 PV_CO_2 × 30 days)	15 psi drawdown	74.2420

production of 73.71 Mbbls at 0.25 pore volume injection of carbon dioxide, that is, at 722 Scf/day.

Quantifying storage/leakage

Initially, carbon dioxide was injected within each sand unit in accordance with the predetermined optimum injection pressure of 722 Scf/day, to maximize oil recovery. The producers were allowed to operate until a 'fall-off' in oil production rate was observed. The dates corresponding to these 'fall offs' in production rate were retrieved from a plot of oil rate in barrels per day versus time in days. These dates were then used as the shut-in dates for each respective producer. The injector shut-in dates were correlated to the time taken to inject a specific volume of carbon dioxide into the storage formation. In our case, we investigated the maximum capacity of the storage formation by computing the time taken to occupy one pore volume at the optimum injection rate of 722 Scf/day. This 1 pore volume maximum capacity of the storage formation was regarded as a conservative limit. Such a conservative approach is taken so as to ensure that injection activities do not propagate hydraulic fractures within our reservoir and thus stimulate leakage. The resulting calculation can be observed below.

Total pore volume of sector model; 193.301 MMScf = 1 PV
Injection rate = 722 Scf/day/Inj
Total number of injectors within sector; 14
Injection duration to occupy 1 PV = $\frac{193.301\times10^{6}\ \text{Scf}}{365\ \text{Days}\times14\ \text{Inj}\times722\ \text{Scf/Day/Inj}} = 52.39 \approx 53\ \text{Years}$

As a result, all injectors were shut-in after 53 years of carbon dioxide injection. The producer located at the topmost layer was then opened to production, and the model was allowed to run for 88 years to observe the action of various trapping mechanisms at work. For the modelling of trapping due to hysteresis, the Holt'z equation was used to compute a value for maximum residual gas saturation. The resultant calculation can be observed in the following few lines;

$$\text{Maximum residual gas saturation } (S_{grm}) = -0.9696\emptyset + 0.5473$$
$$S_{grm} = -0.9696(0.27) + 0.5473$$
$$S_{grm} = 0.285508$$

Following this operation outlined above, the simulation run was implemented which saw the producer at the topmost sand layer of the sector model not registering a gas rate, and thus it was concluded that leakage of the injected carbon dioxide did not occur. However, it is expected that some of the injected carbon dioxide was produced during the EOR process. In light of such, a mass balance approach was undertaken to quantify the volume of injected carbon dioxide, which remained within the reservoir. From Fig. 10, we observe the total amount of carbon dioxide injected, and the total amount produced during oil recovery. As a result, the volume of carbon dioxide still present within the formation was equated as the difference between these two values. The resultant calculation can be observed in Table 6, which depicts the total volume of carbon dioxide still present within the storage formation as 177.068 MMScf.

This 177.068 MMScf of gas within the storage formation can now be sub-divided into its constituent volumes associated with the various types of trapping mechanism as discussed in the theory section. As previously mentioned, these trapping mechanisms include dissolution trapping, mineral precipitation, structural trapping, and trapping by hysteresis. The corresponding amounts in pounds, for each type of trapping, can be observed in Fig. 11. This graphical data is also summarized and presented in a tabular manner, as depicted in Table 7. The general trend inferred from comparing each type of trapping on one singular plot shows that the major quantity of trapped carbon dioxide is initially facilitated by trapping in the supercritical phase. This can be attributed to the action of primary trapping mechanisms, such as structural trapping which acts to hold the supercritical carbon dioxide in place. In addition, significantly trapped volumes are also facilitated by trapping present in

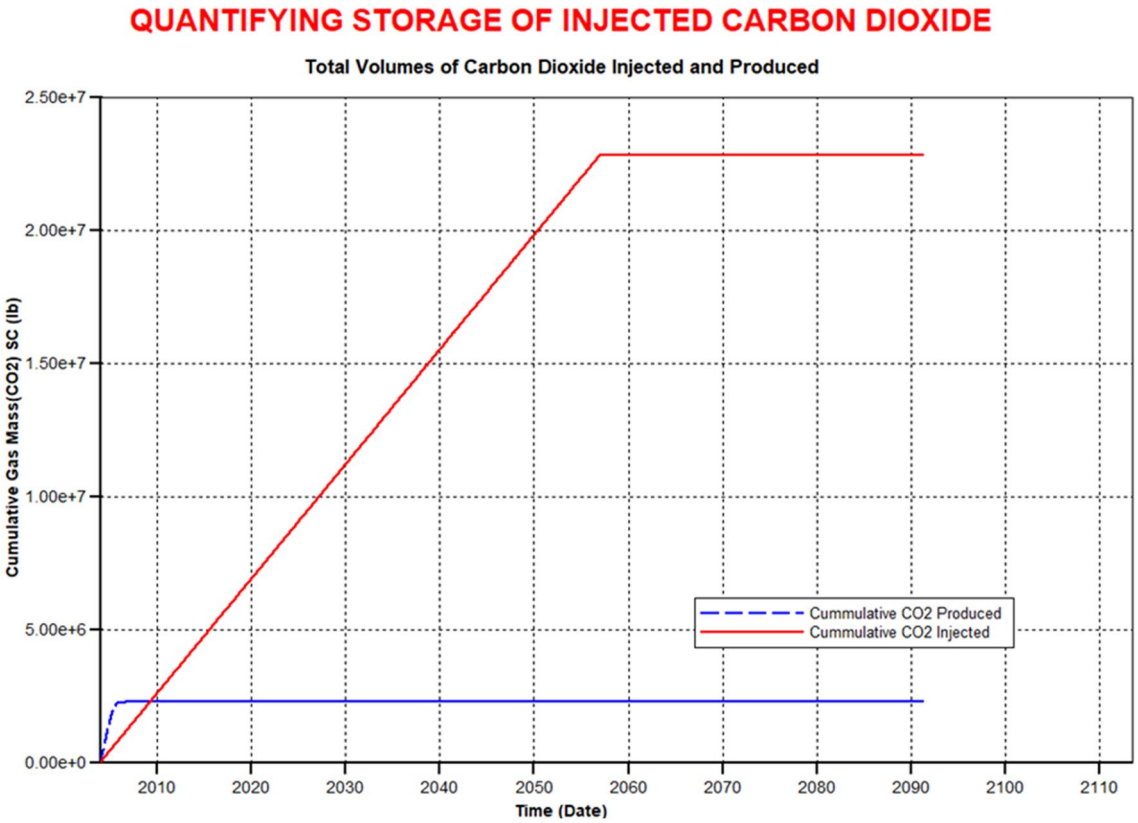

Fig. 10 Illustration of total volume of carbon dioxide injected, and total volume of carbon dioxide produced during combined CO_2 EOR and sequestration

Table 6 Calculation of volume of carbon dioxide present within the reservoir after combined CO_2 EOR and sequestration

Total CO_2 injected	2.28394×10^7 lb
Total CO_2 produced	2.27352×10^6 lb
Total CO_2 present in Res.	2.0565480×10^7 lb
Conversion; 0.00861 MSCF per lb	
Total CO_2 present in Res.	177.068 MMScf

the form of aqueous ions and carbon dioxide dissolved in aqueous state.

These various aforementioned types of trapping cumulatively account for approximately 86% of the total volume of injected carbon dioxide stored. The remaining volume of carbon dioxide is trapped by the action of secondary mechanisms, which typically comes into operation over prolonged periods, usually in the magnitude of thousands of years. Since the study was only conducted over an 88-year period, the action of secondary trapping mechanisms are relatively insignificant and thus accounts for such small amounts of trapping associated with mineralization and dissolution.

Investigating the characteristics of fault reactivation induced by carbon dioxide sequestration

For the Geomechanical study of fault reactivation, a simple two-dimensional block model was constructed to represent a thin two-dimensional homogenous segment of the larger GEM field model. As such, the block model was constructed using the same reservoir, rock, and fluid properties as the field model. The GEM suite was also used as the simulator type, and as a result, the model was also populated with the same Winprop fluid model created previously. The model laterally spans 1010 feet in length by 10 feet in width. Formation thickness is 311.5 feet and considers three impermeable shale layers which act as tops seals for four sand units. The topmost sand unit is capped with an additional 10 feet of impermeable shale and 2.5 feet of sand above this. These two additional layers are not included in the GEM three-dimensional field model and are only incorporated in the 2D segment for the purpose of quantifying leakage associated with fault reactivation. The fault vertically spans the entire thickness of the reservoir and therefore consists of nine grid blocks adjacent to the nine layers of the reservoir.

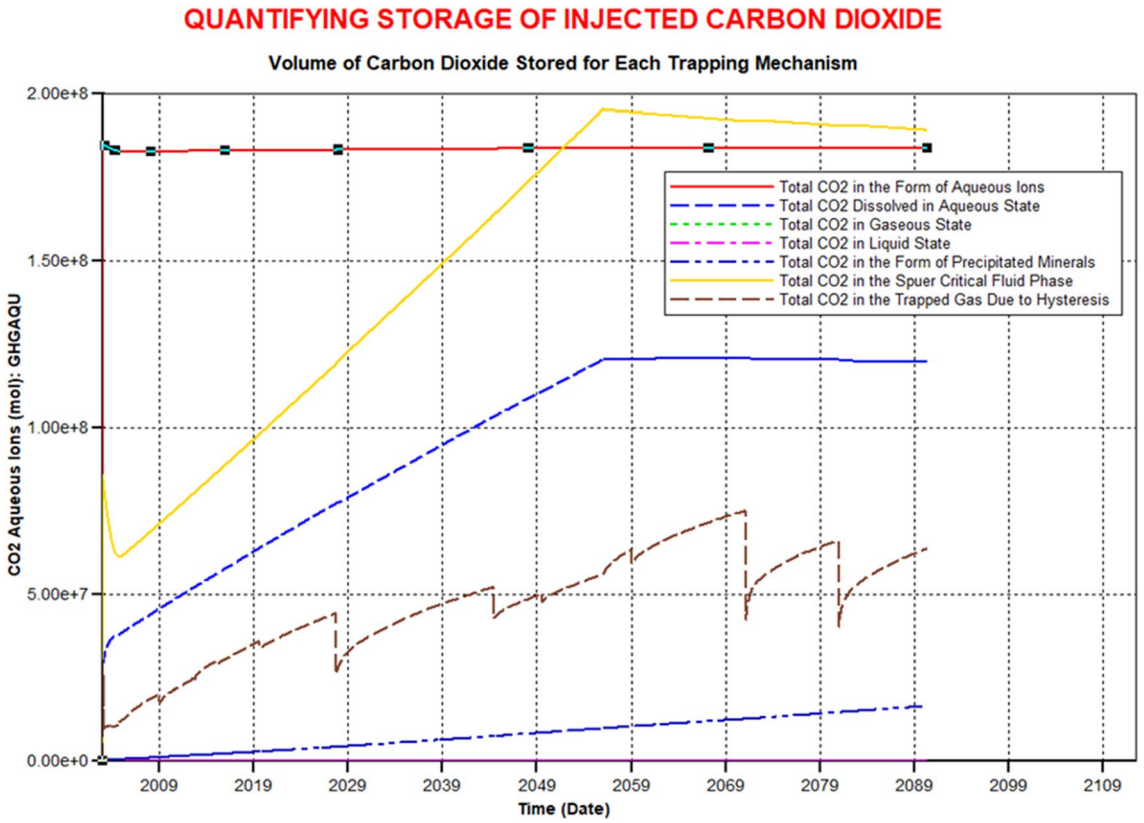

Fig. 11 Illustration of the mass of carbon dioxide stored within the formation for each trapping mechanism

Table 7 Total amounts of carbon dioxide trapped within the reservoir of each corresponding trapping mechanism

Type/phase of storage	Amount (lb)	Amount (MMSCF)
Gaseous	0	0
Liquid	0	0
Supercritical	1.83672E7	158.141592
Hysteresis	6.14064E6	52.8709104
Dissolved (Aqu State)	1.16136E7	99.993096
Aqueous ions	1.78408E7	153.609288
Mineral precipitate	1.57776E6	13.5845136
Conversion; 0.00861 MSCF per lb		

Figure 12 depicts the faulted three-dimensional view of this simple block model. This simplified 2D approach allows for the placement of injectors and/or producers at the periphery of the block model to limit reservoir size or varying degrees of leakiness of the reservoir, which is seen as a significant advantage as compared to the more sophisticated 3D model. Initially, the producer is placed at the topmost layer of the fault to quantify leakage associated with fault reactivation. The injector, however, is approximately 760 feet away from the fault, which is represented by the vertical arrangements of blue grid blocks. The fault is modelled as initially sealing and hence, comprise of a sealing potential which is broadly quantified by the capillary entry pressure and permeability. These are generally regarded to have the most significant impact on leakage, and thus, the dynamic sealing capacity of the fault was modelled and resolved numerically by coupling rock deformation, prompted by reservoir pressurization and modifying fluid flow properties. Typically, the fault would be modelled as connections via assigning transmissibility multipliers to control the amount of flow occurring across and/or through the fault-matrix interface. This type of modelling is preferred when the simulation of fluid transport is the main factor being investigated for the fault.

However, as the modelling of fault reactivation, geomechanics, and the respective changes in permeability form the underlying basis of the study, the modelling approach undertaken for this 2D reservoir model applies a geomechanical based approach to simulate variations of openness within the fault. Such variations are based on increases in hydraulic fracture permeability, influenced by pressurization via carbon dioxide injection. To allow for increases in hydraulic fracture permeability, the 2D model was constructed as a Dual Permeability grid submodel coupled with the 'Barton–Bandis' fracture permeability submodel. Refer to the theory section for the concepts at work for each of the aforementioned submodels used.

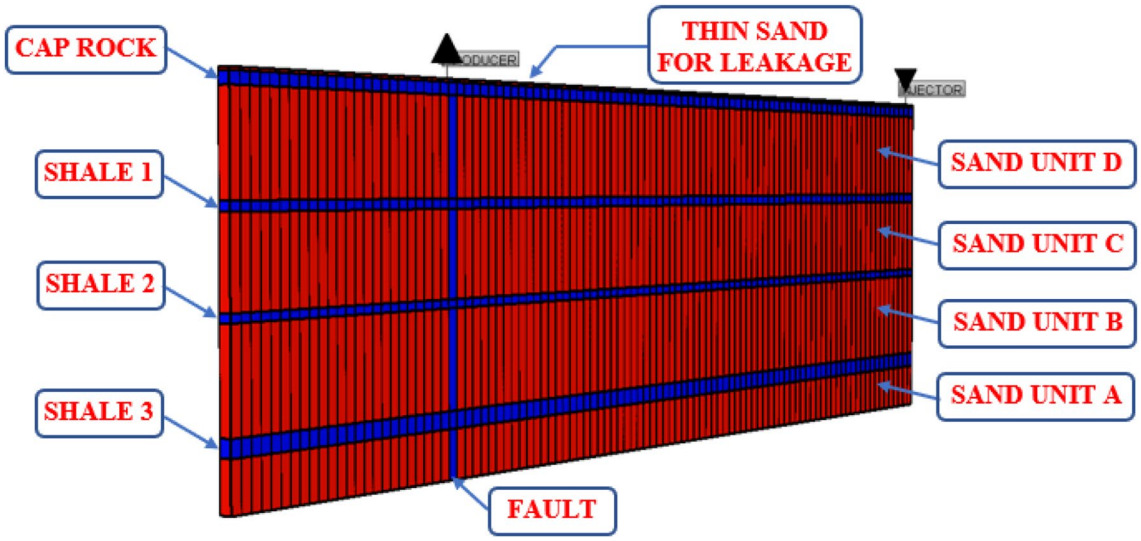

Fig. 12 Three-dimensional view of the 2D homogeneous layered model for geomechanical study of fault reactivation

Fault opening stress

To investigate fracture opening stress, continuous injection of carbon dioxide was implemented on the two-dimensional model at a predetermined injection rate of 722 Scf/day. Initially, gas was injected in the bottommost sand unit and then allowed to pressurize the layer to investigate the occurrence of fault reactivation via the action of the Barton Bandis submodel. Importantly, however, the application of the Barton–Bandis submodel saw the fault reactivating on a grid block basis, as depicted in Fig. 13. Within the following sections, the depicted fault block numbers presented in Fig. 13 will be used to draw reference to a particular portion of the fault to discuss the acquired results.

Despite this, the operation and application of the Barton Bandis submodel required a value be set for fracture opening stress. However, by manually setting this value, we are in essence, controlling fault reactivation and the pressure at which it occurs. As a result, to accurately capture the characteristics of fault reactivation, a sensitivity analysis on fracture opening stress was undertaken. The study entailed carbon dioxide injection at a constant rate of 722 Scf/day over a fifty-year period, at varying fracture opening stresses to observe the effect on the time required for reactivation. Although a duration of fifty years may seem impractical from a recovery standpoint, the study on reactivation is also in regard to sequestration, which typically operates for lengthy periods. The results of the simulation runs are presented and explained below.

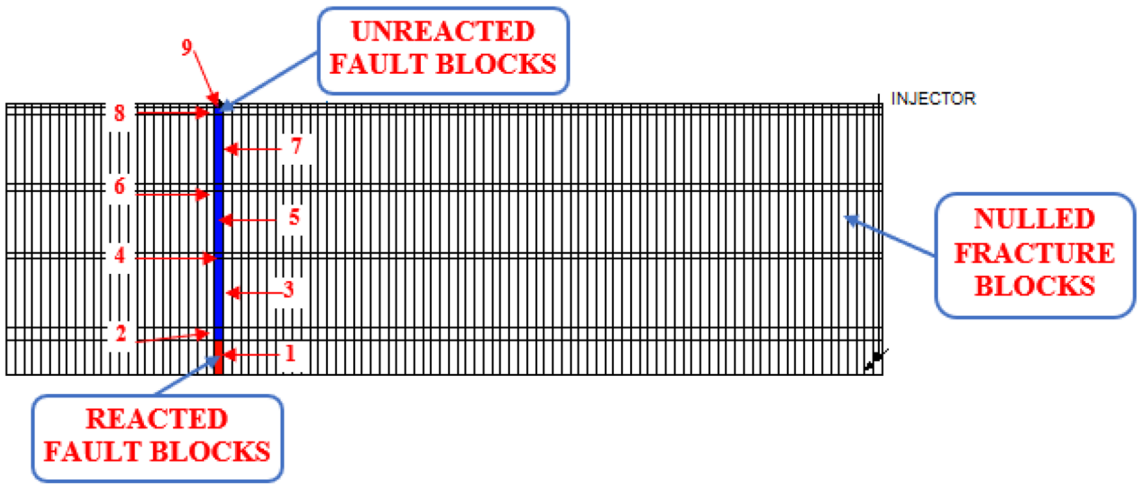

Fig. 13 Illustration of fault reactivation and fault-block numbering for referencing during discussions on reactivation results

Reactivation at base of fault Figure 14 depicts a plot of vertical permeability against time and was used as the analysis to observe the effect of varying fracture opening stresses on fault reactivation time. The permeability axis merely serves as an indication of fault reactivation via an increase in fault/fracture permeability. The basis of the investigation, however, centers on simulating reactivation or the lack thereof, under constant injection at varying fracture opening stresses. These variations of fracture opening stress were observed to have a significant effect on the time taken for fault reactivation. This is confirmed as the fault is observed to undergo reactivation at the base (fault block 1), under a fault opening stress of 25 psi, however, does not reactivate at a fault opening stress of 10 psi. As a result, it can be deduced that under these geomechanical and injection constraints, all faults with fracture opening stresses higher than 25 psi, are expected to undergo fault reactivation. Moreover, the general trend inferred from Fig. 14 is that, as fracture opening stress decreases, the time taken for fault reactivation increases. Therefore, an inverse relationship between the two variables is established, such that, for example, the time taken for reactivation at fracture opening stress equals 510 psi, is approximately half the time taken for reactivation at fracture opening stress equals 300 psi. This trend can be attributed to the mechanism of the Barton–Bandis submodel and the relationship between normal effective stress and pore pressure within a specific grid block. The latter relationship is defined as described in the equation below, which states that normal effective stress (σ') is computed as the difference in the normal stress (σ) and pore pressure (P_p) at any given instance. That is;

$$\sigma' = \sigma - P_p$$

From the above relationship, it can be inferred that as pore pressure increases, normal effective stress decreases. Since injection was simulated at a constant rate, this infers a constant increase in pore pressure for all simulation runs. Such a constant increase in pore pressure thus infers a constant decrease in normal effective stress. Complimentary to this, recall that such a decrease in normal effective stress forms the basis of operation of the Barton–Bandis submodel. That is, an increase in fracture permeability (which is indicative of fault reactivation) is prompted when the normal effective stress decreases so much so that it equates or becomes less than the fracture opening stress. Therefore, as we are increasing fault opening stress, we are essentially decreasing the difference between normal effective stress

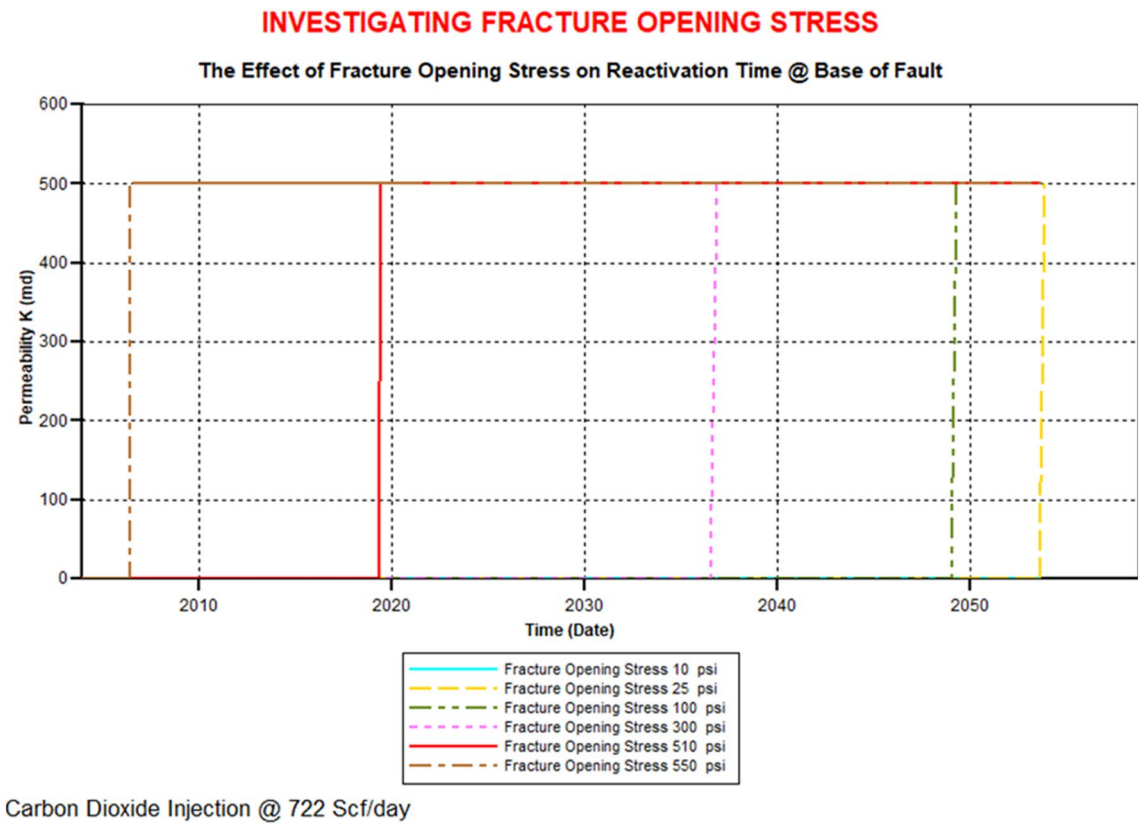

Fig. 14 Time taken for the onset of fault reactivation at the base of the fault for varying fracture opening stresses

and fault opening stress. This reduction in the difference between the two stresses thus infers a smaller value of pore pressure required to reduce the normal effective stress to equate or become less than the fracture opening stress, that is, to prompt reactivation. This lesser value of pore pressure requires less injection for reactivation and thus translates to a faster reactivation time. Likewise, the opposite occurs when fracture opening stress is decreased, and therefore accounts for the trend observed within Fig. 14.

Reactivation at the top of fault In addition to investigating reactivation at the base of the fault, an analysis was undertaken at the topmost fault block, that is, at fault block nine. The primary purpose of this study was to investigate the occurrence, or lack thereof, of fracture propagation along the entire thickness of the reservoir. This also forms an integral part of a subsequent investigation into the leakage associated with reactivation. As a result, the occurrence of reactivation was observed by a similar plot of vertical permeability against time. The result of this study can be observed in Fig. 15. From the respective plot, only two instances of fracture propagation were observed to have affected the topmost layer of the formation (fault block 9). These were seen to occur at 540 psi and 545 psi, respectively, that is, at the largest values of fracture opening stress. As a result, it can be deduced that at values of fracture opening stress less than 540 psi, the fault undergoes partial reactivation and leakage does not reach the topmost layer of the reservoir.

Comparing reactivation at the base of the fault, to the top of the fault In addition, a comparison of the reactivation times for the base fault block, as opposed to reactivation at the uppermost fault block, was made. This difference in reactivation time gives an indication of the time taken for the fracture to vertically propagate throughout the entire length of the reservoir. The result of this study can be observed in Fig. 16. It was observed that as fracture opening stress increased, the time taken for the fracture to vertically propagate through the entire length of the reservoir decreased. Once more this can be attributed to the explanation given within the previous discussion with regards to Fig. 14. But perhaps the major piece of information obtained from these results, are the respective times taken for complete reactivation which are tabulated in Table 8. In light of this information, reactivation can now be induced via injection, in an attempt to reactivate the lower faults blocks, however, halting injection before reactivation time at the uppermost fault block is reached. This approach, therefore, allows access to the maximum capacity of the formation without compromising the integrity of the pre-existing topmost seal

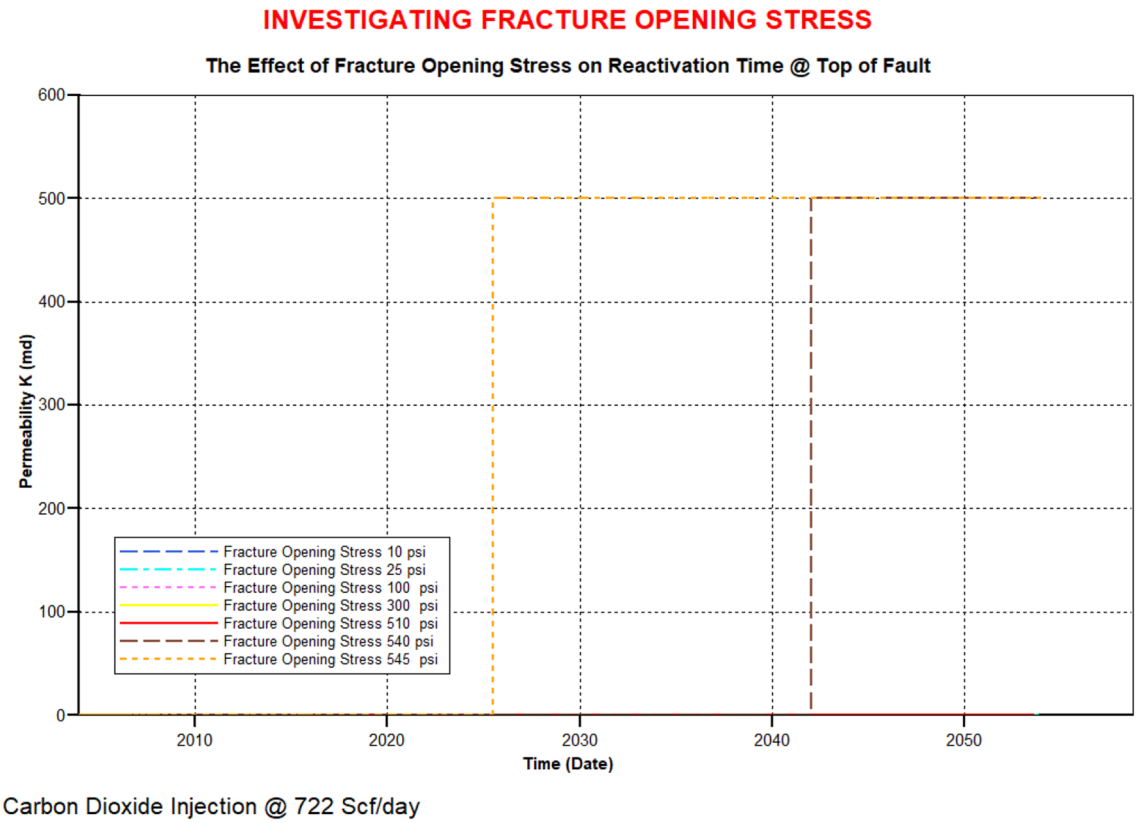

Fig. 15 Time taken for onset of fault reactivation at the top of the fault for varying fracture opening stresses

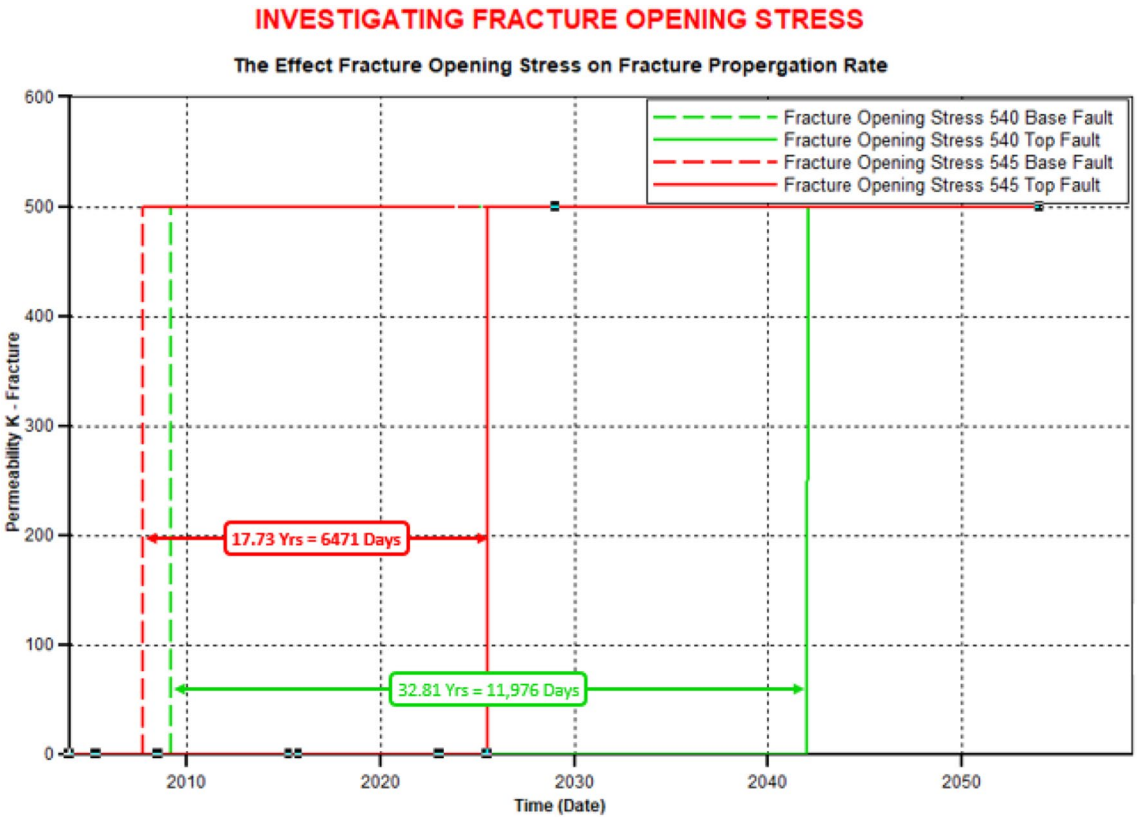

Fig. 16 Time taken for complete fracture propagation throughout the vertical thickness of the reservoir

Table 8 Time taken for complete reactivation along the entire length of the fault

	Date of reactivation	
	FOS = 540 PSI	FOS = 545 PSI
Base of fault	2009-3-6 1904th day	2007-9-28 1380th day
Top of fault	2041-12-18 13880th day	2025-6-16 7851th day
Time for full reactivation	11,976 Days = 32.81 Years	6471 Days = 17.73 Years

and hence, increases storage volumes. A depiction of this increase in storage capacity is depicted in Fig. 17.

The effect of hydraulic fracture permeability at the base and top of the fault

The investigation of hydraulic fracture permeability was conducted on the basis of observing the effect of hydraulic fracture permeability on the time taken for total fracture propagation throughout the thickness of the reservoir. As a result, for this purpose, a model with a fracture opening stress which resulted in total vertical fracture propagation throughout the entire thickness of the reservoir was utilized. This model was retrieved from the previously conducted study on 'the time taken for reactivation at the top of the fault (fault block 9)' which corresponds to a fracture opening stress of 545 psi. The injection strategy remained the same, as carbon dioxide was injected at the bottommost layer and a constant rate of 722 Scf/day. The time taken for reactivation to occur at bottommost and topmost fault blocks (fault blocks 1 and 9, respectively) was then observed. Figure 18 depicts the time taken for reactivation to occur at the base of the fault for varying fault reactivation permeabilities. From this plot, we observe that the time taken for reactivation at the base of the fault was constant for each varying case of hydraulic fracture permeability. That is, reactivation at the base of the fault occurs at the same instance of time, regardless of the hydraulic fracture permeability. This trend can be attributed to the fact that the fracture opening stress was held constant at 545 psi under a constant injection rate of 722 Scf/day, and no alterations in the permeability of the surrounding matrix were made. Therefore, at the base, the fault is exposed to precisely the same pressure build-up profile for each varying case of hydraulic fracture permeability and hence undergoes reactivation at the same point for each case.

On the other hand, it was observed from Fig. 19, that varying hydraulic fracture permeability does affect the time taken for reactivation at the top of the fault. The general trend inferred from the resultant plot relates a decrease in

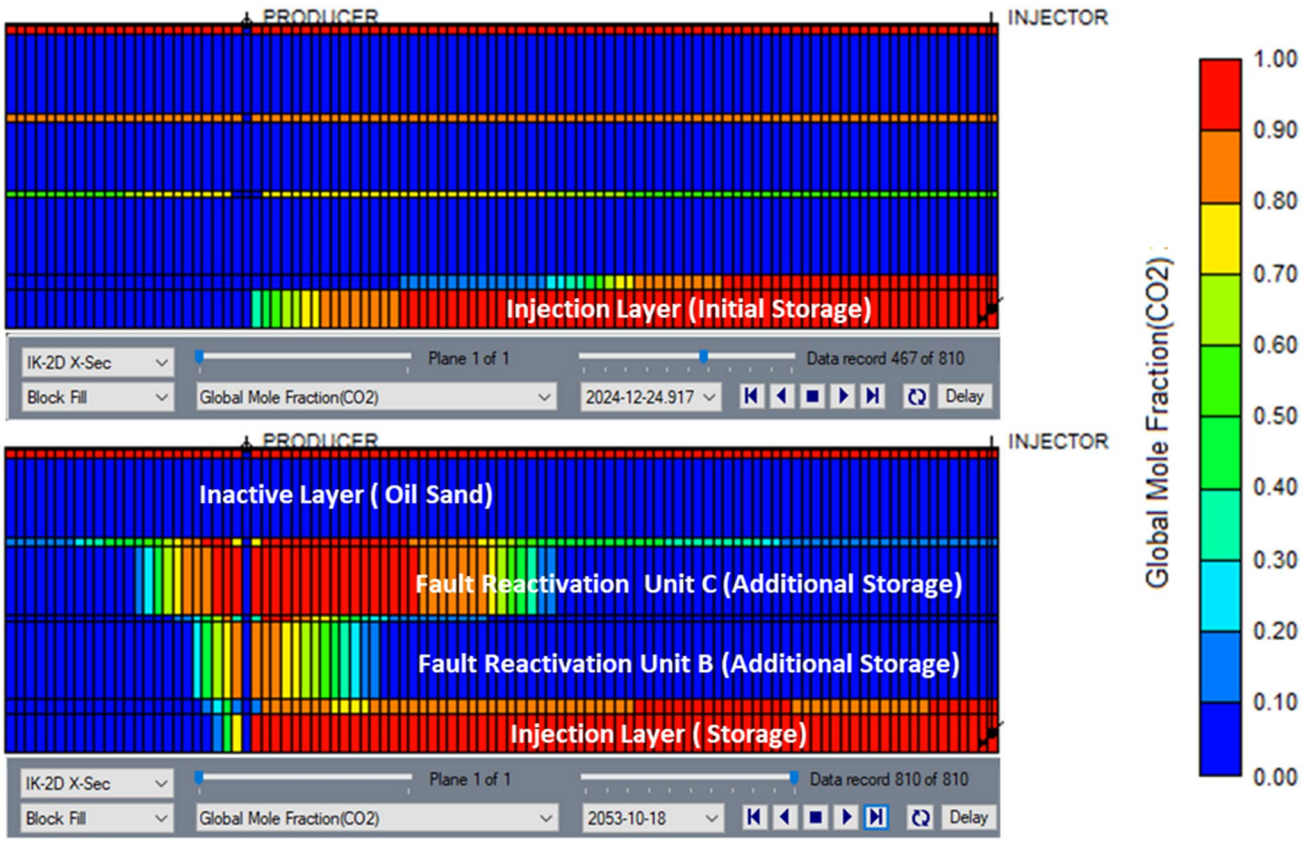

Fig. 17 Depiction of an increase in storage volume for carbon dioxide due to fault reactivation

time taken for reactivation with an increase in hydraulic fracture permeability. From the plot, we see that at values of hydraulic fracture permeability greater than 100 md, reactivation at the top generally occurs around the same time. However, at the lower end values of 50 md and 10 md, respectively, reactivation occurred after a prolonged period, relative to the other instances. Such a trend can be attributed to the pressure build-up throughout the fault as it undergoes reactivation. This pressure build-up however is directly related to the reactivated permeability which controls the supply of fluid to the fault blocks.

In our case, at higher values of hydraulic fracture permeability, more carbon dioxide is supplied to the resultant fault blocks, and thus, the pressure build-up occurs at a higher rate as compared to at a lower value of hydraulic fracture permeability. As a result of this higher rate of pressure build-up, the decrease in normal effective stress associated with the Barton–Bandis submodel also occurs at a higher rate. This, therefore, allows the normal effective stress acting on the fault to equate to the fracture opening stress within less time, thus resulting in an earlier reactivation.

The effect of hydraulic fracture permeability on leakage of injected carbon dioxide

The study into the effect of varying hydraulic fracture permeability on carbon dioxide leakage entailed the simulation of complete fault reactivation throughout the entire thickness of the reservoir. The basis behind this approach was to quantify the volume of injected carbon dioxide which leaked from the storage layers into the fault and up to the topmost, thin sand layer (refer to Fig. 12). As a result, a model which simulated complete fault reactivation up to the fault block 9 was utilized. As such, the study was implemented by building on the results of the previous study (the effect of hydraulic fracture permeability on time of reactivation), and thus the same model was utilized, that is, the model with fracture opening stress of 545 psi. Initially, the addition of a producer to the topmost fault block was implemented. The purpose of this producer was to quantify the amount of leakage associated with the occurrence of fault reactivation. In essence, however, to accurately quantify the amount of leakage which occurs after the onset of fault reactivation, the injection should be halted, to prevent the flushing of free carbon dioxide gas by continuous injection. As a result, the injector within our model was shut-in, in accordance with

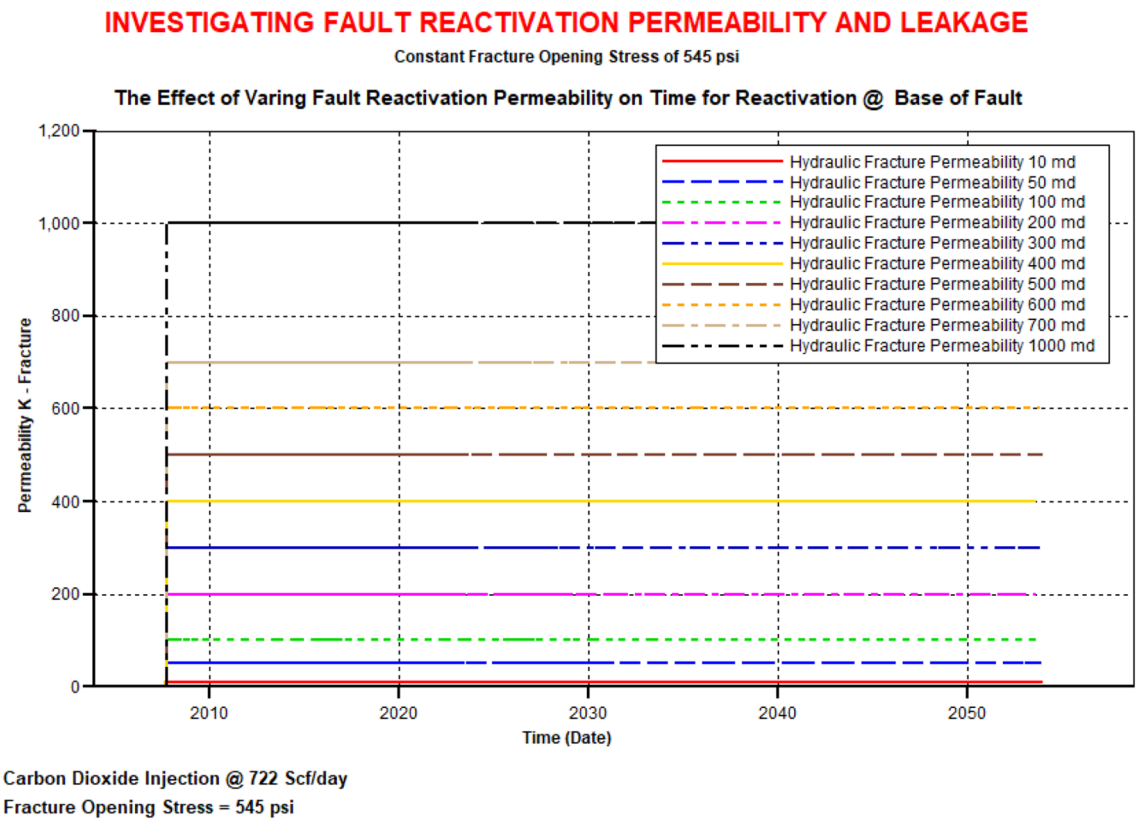

Fig. 18 The effect of varying hydraulic fracture permeability on the time taken for reactivation at the base of the fault

the respective reactivation times for each model of varying hydraulic fracture permeability. These results of reactivation time were retrieved from the previous study via Fig. 19. A summary of these shut-in dates retrieved and used for the study can be observed in Table 9.

An exemplary, arbitrary depiction of the simulation setup for quantifying model leakage in the 2D block model is presented via Fig. 20. From this, a general idea of the operation of the model can be gained, which is as follows. Initially, carbon dioxide injection is implemented at the base layer at an injection rate of 722 Scf/day, represented by the blue curve as observed in Fig. 20. At the point of fault reactivation (indicated by an increase in fracture permeability) at the topmost fault block, represented by the green curve on Fig. 20, injection is halted. Simultaneous to this, the producer located at the topmost layer, perforated within the topmost fault block (fault block 9) is opened for production. This producer then quantifies the total volume of injected carbon dioxide (represented by the red curve on Fig. 20) which makes its way up through the fault and to the topmost layer.

Likewise, under the same model operation at varying hydraulic fracture permeabilities, the effect of hydraulic fracture permeability on the volume of injected carbon dioxide leaked was assessed. From the resulting plot, Fig. 21, the general trend observed was, as hydraulic fracture permeability increased, the volume of injected carbon dioxide leaked also increased. Such a trend is expected as hydraulic fracture permeability is a direct representation of the fault's ability to conduct fluid flow upon reactivation. As such, instances where reactivation resulted in larger reactivated fault permeabilities, the volume of injected carbon dioxide allowed to flow through the fracture was greater than the volume at lower values of reactivated permeabilities. This pattern can be clearly observed by tabulating the cumulative volumes of injected carbon dioxide leaked.

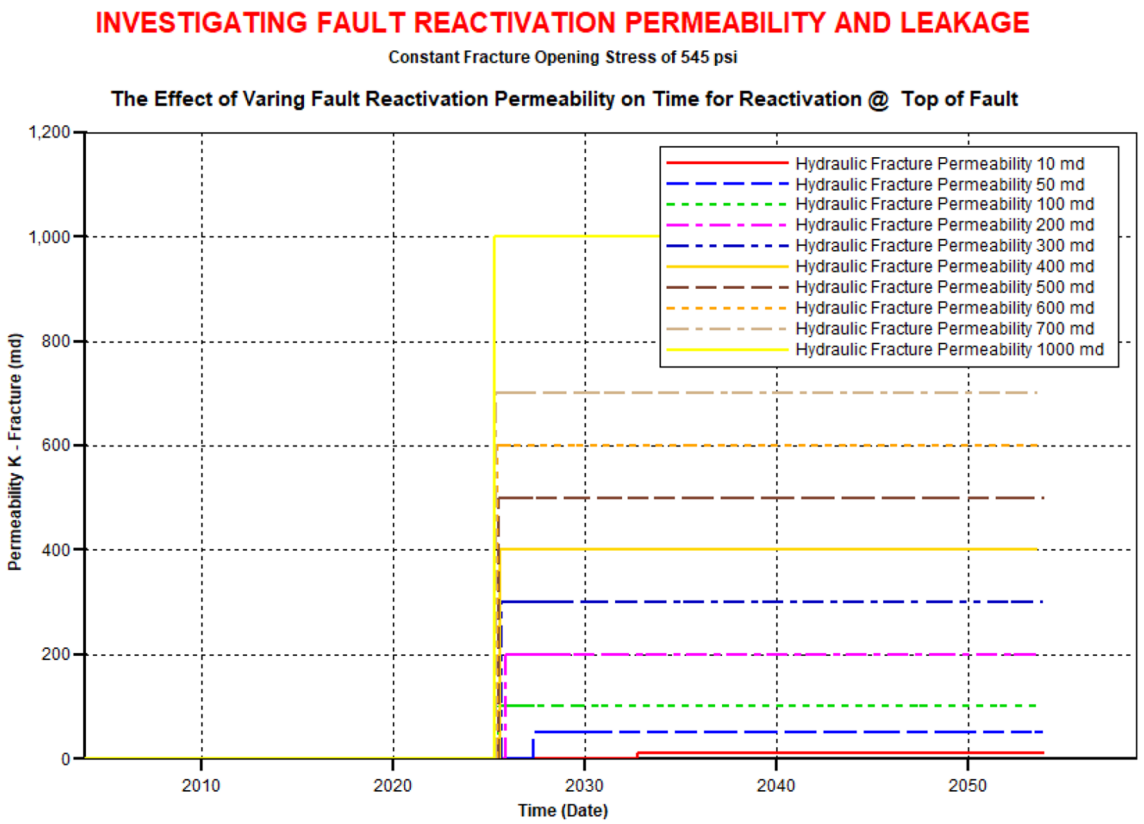

Fig. 19 The effect of varying hydraulic fracture permeability on the time taken for reactivation at the top of the fault

From Table 10, we observed that at a hydraulic fracture permeability of 200 md, the total volume of injected carbon dioxide leaked amounted to approximately twice the amount leaked at a hydraulic fracture permeability of 10 md. However, the total volume of injected carbon dioxide leaked was observed to remain practically constant at values of hydraulic fracture permeability greater than or equal to 100 md. This trend can be attributed to the reactivation times determined in the previous study. That is, from Table 9, we see that for the faults with hydraulic fracture permeability greater than or equal to 100 md, the time taken for reactivation is relatively the constant (within the same year). Whereas, for the faults with hydraulic fracture permeability less than this, that is at 50 md and 10 md, respectively, fault reactivation was experienced at subsequent years. This reactivation at subsequent years thus infers that a shorter time for leakage is allowed. This coupled with the comparatively lower ability to transmit fluid (lower hydraulic fracture permeability), therefore accounts for such lower values of leakage.

Conclusion

The investigation into the combined processes of carbon dioxide enhanced oil recovery, and geologic carbon sequestration was seen to be a viable solution to reducing carbon dioxide emissions from the atmosphere while boosting production form mature oil fields. From studies conducted, we saw that it was possible to stimulate additional oil recovery within a 3D GEM sector model, representative of mature oil filed via continuous injection. A cumulative production of 73.7090 MBbls was associated with the enhanced recovery aspect of the project, while sequestration of 177.068 MMScf of carbon dioxide was achieved, without any trace of leakage over a 32-year monitory period. However, on the opposing spectrum,

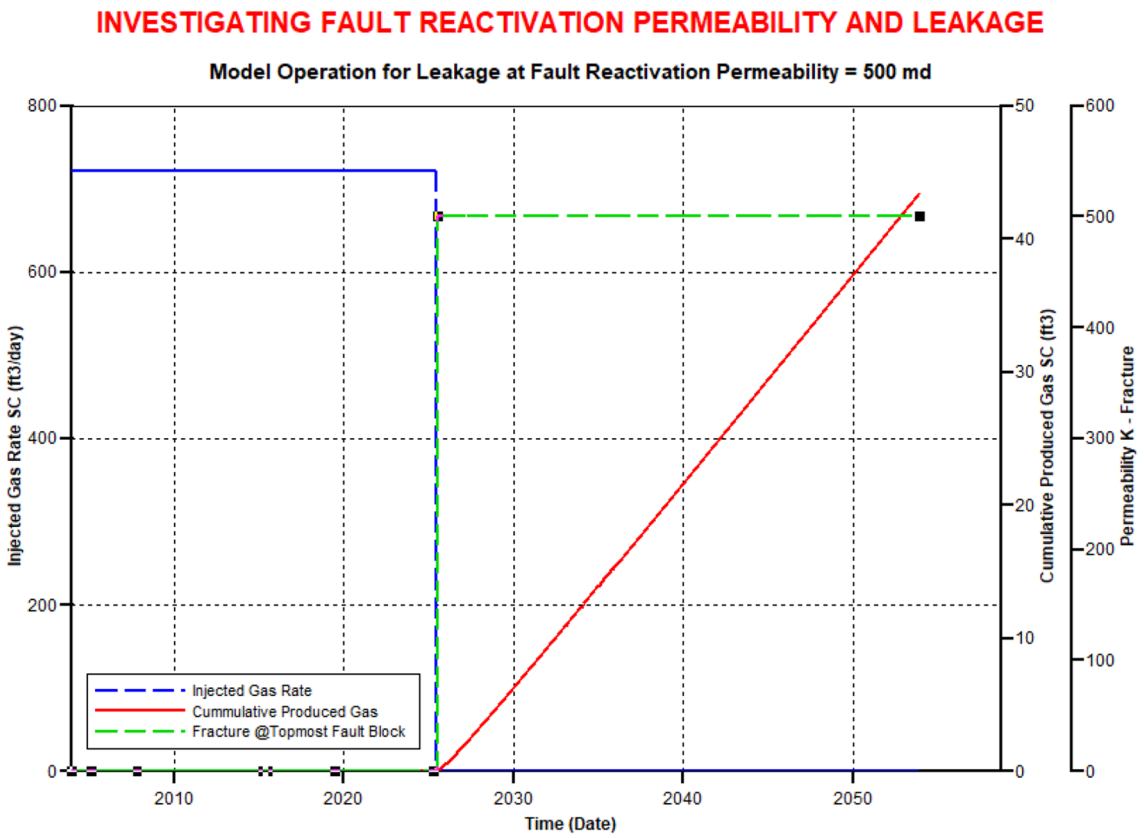

Fig. 20 Model operation for quantifying leakage of injected carbon dioxide at hydraulic fracture permeability of 500 md

injection of carbon dioxide for the intentions of sequestration was also observed to induce fault reactivation, albeit under specific cases of rock mechanics and fracture properties within a 2D block model. The method of investigation utilized to simulate fault reactivation was regarded as the Barton–Bandis model and gave a simple approach to coupling fault mechanics to fluid flow operations. It allows a primary option to investigate the characteristics of fault reactivation, however under a two-dimensional constraint. If a more dynamic approach to simulating fault reactivation is required, a more complex simulation option should be employed. Moreover, the use of the Barton–Bandis option allowed the simulation of vertical fault reactivation on a fault block basis. As a result of this, some underlying trends associated with the process of fault reactivation were noted. These included;

1. The relation of fracture opening stress with the reactivation time. Generally, as fracture opening stress increased, time taken for fault reactivation decreased.
2. As pore pressure increased via carbon dioxide injection, a decrease in effective normal stress is observed according to the relationship here; $\sigma_n' = \sigma - P_p$.
3. In certain instances, the fault underwent partial reactivation, which in turn increased the storage capacity of the reservoir.
4. The time taken for the fracture to propagate the entire length of the formation can be determined by observing the reactivation times at the topmost and bottommost fault blocks.
5. The time taken for the fracture to propagate the entire length of the formation was seen to be affected by hydraulic fracture permeability. Generally, as hydraulic fracture permeability increased, the time taken for the

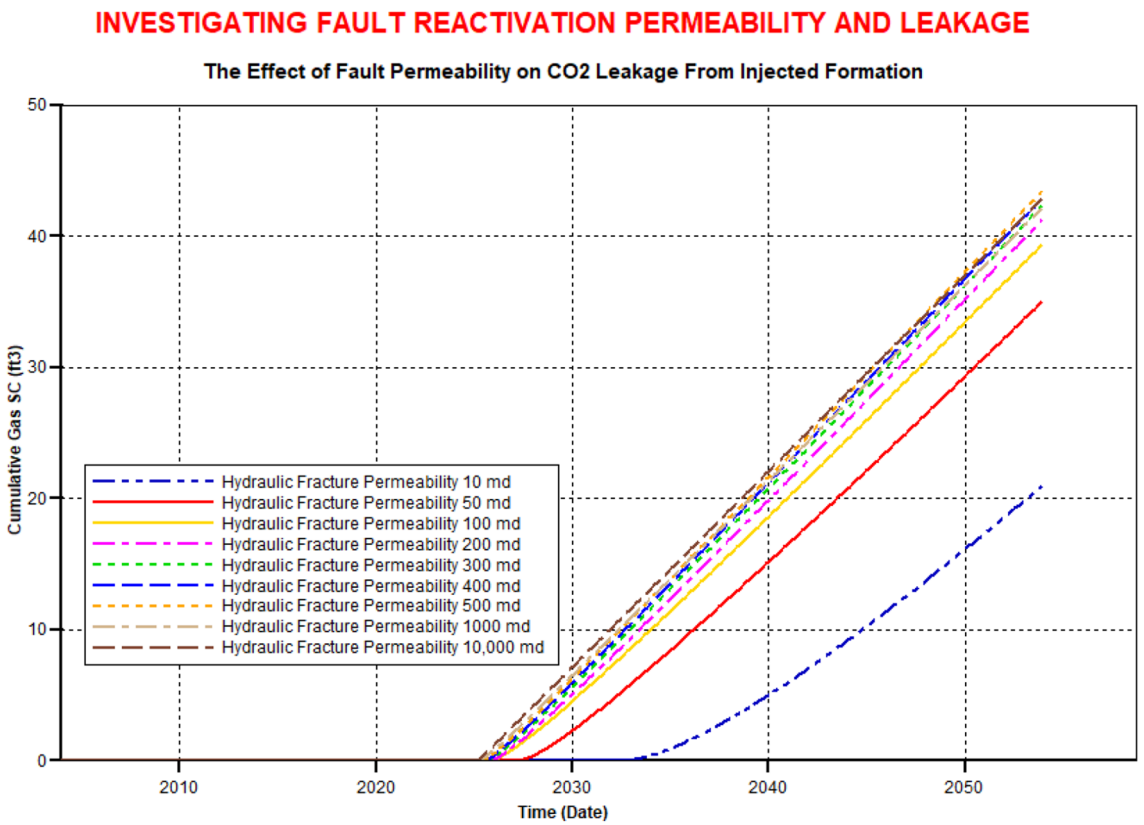

Fig. 21 Leakage volumes of injected carbon dioxide associated with reactivation at the topmost fault block, at varying hydraulic fracture permeabilities

Table 9 Values of fault reactivation time at the topmost fault block, which corresponds to the injection well shut-in dates

Varying hydraulic fracture permeability models	Time of reactivation = shut-in date
10 md	2032-9-17
50 md	2027-3-30
100 md	2025-6-3
200 md	2025-12-1
300 md	2025-8-18
400 md	2025-8-18
500 md	2025-6-3
1000 md	2025-1-30

Table 10 Quantities of injected carbon dioxide leaked at corresponding fault reactivation permeabilities

Fault reactivation permeability	Total volume injected of CO_2 leaked (Scf)
10 md	20.99
50 md	35.07
100 md	39.42
200 md	41.27
300 md	42.37
400 md	42.94
500 md	43.48
1000 md	42.19

fracture to propagate the entire length of the formation decreases.

6. As fault reactivation permeability increased, the volume of injected carbon dioxide which travels to the surface also increases, that is, an increase in leakage.

References

Advanced Resources International and Melzer Consulting (2010) Optimization of CO_2 storage in CO_2 enhanced oil recovery projects

C.M.G Ltd (2016) Gem user guide—compositional & unconventional reservoir simulation, version 2016. Computer Modeling Group Ltd, Calgary

Knoema (2019) Trinidaad and Tobago—proved reserves of natural gas. Retrieved from Knoema Corporation: https://knoema.com/atlas/Trinidad-and-Tobago/topics/Energy/Gas/Reserves-of-natural-gas. Accessed 3 Oct 2019

Sobers LE, Blunt MJ, LaForce TC (2011) Design of simultaneous enhanced oil recovery and carbon dioxide storage applied to a heavy oil field offshore Trinidad. In: SPE annual technical conference & exhibition, Denver, Colorado, USA. Society of Petroleum Engineers, pp 1–11

Ramlal V (2004) Enhanced oil recovery by steamflooding in a recent steamflood project, cruse 'E' field, Trinidad. Soc Pet Eng 1–15

The Global Carbon Atlas (2018) CO_2 emissions. Retrieved from The Global Carbon Atlas. http://www.globalcarbonatlas.org/en/CO2-emissions. Accessed 29 Sept 2019

The National Gas Company of Trinidad and Tobago (2019) CASCO News. NGC Group Companies Corp Q J 29(1):1–30